
CRYSTALLOGRAPHIC TEXTURE–GENERALIZABLE ORIENTATION-AWARE INTERACTION-BASED DEEP MATERIAL NETWORK FOR POLYCRYSTAL MODELING AND TEXTURE EVOLUTION

Ting-Ju Wei

Department of Civil Engineering
National Taiwan University
Taipei, Taiwan

Tung-Huan Su*

ANSYS Inc.
Livermore, CA, USA

Chuin-Shan Chen†

Department of Civil Engineering
Department of Materials Science and Engineering
National Taiwan University
Taipei, Taiwan

December 9, 2025

ABSTRACT

Machine learning has significantly advanced materials modeling by enabling surrogate models that achieve high computational efficiency without compromising predictive accuracy. The Orientation-aware Interaction-based Deep Material Network (ODMN) is one such framework, in which a set of material nodes represent crystallographic textures, and a hierarchical interaction network enforces stress equilibrium among these nodes based on the Hill–Mandel condition. Using only linear elastic stiffness data, ODMN learns the intrinsic geometry–mechanics relationships within polycrystalline microstructures, allowing it to predict nonlinear mechanical responses and texture evolution with high fidelity. However, its applicability remains limited by the need to retrain for each distinct crystallographic texture. To address this limitation, we introduce the TACS–GNN–ODMN framework, which integrates (i) a Texture-Adaptive Clustering and Sampling (TACS) scheme for initializing texture-related parameters and (ii) a Graph Neural Network (GNN) for predicting stress-equilibrium-related parameters. The proposed framework accurately predicts nonlinear responses and texture evolution across diverse textures, showing close agreement with direct numerical simulations (DNS). By eliminating the requirement for texture-specific retraining while preserving physical interpretability, TACS–GNN–ODMN substantially enhances the generalization capability of ODMN, offering a robust and efficient surrogate model for multiscale simulations and next-generation materials design.

Keywords Crystal plasticity · Deep material network · Graph neural network · Multiscale simulations · Texture Evolution

1 Introduction

Crystal plasticity (CP) is a powerful computational approach for simulating the mechanical behavior of polycrystalline materials. It captures intragranular deformation heterogeneity and enables the prediction of texture evolution under various loading conditions [1, 2]. To bridge the micro-to-macro transition, various homogenization models have been developed. Among them, the classical Taylor model assumes uniform deformation across all constituent grains, which often leads to overestimated flow stresses and exaggerated texture sensitivity [3, 4]. The self-consistent model improves upon this by embedding each grain as an ellipsoidal inclusion within an effective medium [5, 6, 7], yet still lacks the ability to resolve local field fluctuations and grain-to-grain interactions. The relaxed grain cluster (RGC) model

*Corresponding author. Email: michael.su@ansys.com

†Corresponding author. Email: dchen@ntu.edu.tw

addresses this limitation by introducing localized grain clusters and relaxation vectors to account for mismatch at grain boundaries [8, 9], but its reliance on empirically fitted penalty parameters constrains its transferability and robustness.

To overcome the limitations of mean-field models, full-field CP approaches have been developed by discretizing the representative volume element (RVE) into finite elements or spectral voxels. These models, implemented via finite element methods (FEM) or fast Fourier transform (FFT)-based solvers, directly solve the governing equations of mechanical equilibrium and crystal plasticity at the microscale [10, 11, 12, 13, 14, 15]. Their high predictive accuracy has facilitated detailed investigations into dislocation mechanisms, slip system activity, and crystallographic anisotropy [16, 17, 18, 19, 20, 21, 22]. Nevertheless, the substantial computational cost associated with full-field simulations remains a critical bottleneck to their application in large-scale engineering design, process optimization, and real-time prediction scenarios.

To address these challenges, data-driven surrogate models have emerged as promising alternatives in crystal plasticity. These models learn the mapping from microstructural features to macroscopic responses using data generated from high-fidelity simulations. This paradigm offers orders-of-magnitude acceleration during inference while preserving the essential physical characteristics of material behavior.

Recent developments include the use of fully connected neural networks (FCNNs) to predict microstructural evolution and update the macroscale parameters of J2–J3 constitutive models, serving as surrogates for computationally expensive cellular automata–crystal plasticity finite element method (CA–CPFEM) simulations [23]. FCNNs have also been applied to model stress–strain responses and texture evolution of FCC single crystals under various loading paths, and extended to polycrystalline aggregates via Taylor-type homogenization [24]. In addition, physics-constrained neural networks have been proposed by embedding slip system shear–resistance relations directly into the loss function, improving generalization and enabling application to polycrystals [25]. Beyond FCNNs, recurrent neural network (RNN)-based frameworks such as the Linearized Minimal State Cell (LMSC) have been developed to capture history-dependent behavior in FCC polycrystals and demonstrated successful two-scale simulations [26, 27]. Building on LMSC concepts, a temporal graph neural network (TGNN) architecture has recently been introduced, where grain-level deformation and local interactions are encoded by a graph neural network (GNN), and the extracted features are passed to LMSCs to predict the time-dependent stress–strain response and orientation evolution of individual grains [28].

For polycrystalline aggregates, TGNN provides a data-driven description of orientation-dependent grain responses based on a Taylor-type mean-field approximation. In contrast, Deep Material Networks (DMNs) offer a physically interpretable framework for multiscale homogenization, where each bottom node represents a material subdomain of the representative volume element (RVE), and the entire network forms a physics-constrained hierarchy that captures the homogenized behavior of the microstructure [29, 30, 31]. DMNs are trained offline using linear elastic stiffness datasets, allowing the network to learn the intrinsic geometry–mechanics relationships of the RVE through its hierarchical architecture. During online prediction, analytically derived upscaling and downscaling operators ensure equilibrium and compatibility across all building blocks. Consequently, DMNs can efficiently predict nonlinear material responses under arbitrary loading paths across diverse material systems [32, 33, 34, 35, 36, 37].

As a variant of DMNs tailored for polycrystalline materials, the Orientation-aware interaction-based Deep Material Network (ODMN) incorporates crystallographic orientation awareness into the micromechanical hierarchy. This enables the prediction of both stress–strain responses and texture evolution in polycrystalline aggregates using crystal plasticity [38]. However, the original ODMN framework lacks transferability: it must be retrained for each new microstructure, which limits its practical applicability.

To overcome this limitation, we propose the TACS–GNN–ODMN framework, which enhances the original ODMN with two key components: (i) a Texture-Adaptive Clustering and Sampling (TACS) scheme for initializing parameters representing crystallographic textures [39], and (ii) a graph neural network (GNN) for learning parameters governing hierarchical micromechanical equilibrium through grain-level interaction graphs. This integration allows the model to generalize across diverse texture distributions without retraining, while preserving the inherent physical consistency of the ODMN. Numerical experiments demonstrate that TACS–GNN–ODMN accurately predicts both homogenized mechanical responses and texture evolution for previously unseen RVEs, highlighting its strong generalization capability across a wide range of polycrystalline microstructures.

The remainder of this paper is organized as follows. Section 2 introduces the TACS-GNN-ODMN architecture, beginning with a brief overview of the original ODMN formulation, followed by the construction of polycrystal graphs, the design of the GNN architecture, and the TACS initialization strategy. We also describe the dataset used and outline the procedures for offline training and online prediction. Section 3 presents a case study involving four previously unseen RVEs subjected to various loading conditions, where both stress–strain responses and texture evolution are evaluated. Finally, Section 4 summarizes the key findings and concludes the paper.

2 TACS–GNN–ODMN Framework

This section outlines the TACS–GNN–ODMN architecture (Fig. 1), which operates in two stages: offline training and online prediction. During offline training, TACS generates sampled Tait–Bryan angles that accurately reconstruct the orientation distribution function (ODF), providing robust initialization for the texture-related parameters of the ODMN. In parallel, the GNN learns the mapping from grain-level microstructure graphs, where nodes encode attributes such as crystallographic orientation and volume fraction, and edges represent topological adjacency, to the parameters that govern the hierarchical micromechanical equilibrium within the ODMN. The overall framework trains the parametric ODMN in an end-to-end manner to perform the homogenization mapping from constituent elastic stiffness tensors to their corresponding homogenized counterparts, with the latter obtained from full-field numerical homogenization serving as the ground truth.

During online prediction stage, the framework converts an unseen RVE into a grain-level graph, applies the trained GNN to infer the micromechanical equilibrium parameters, and integrates them with the TACS-initialized texture parameters to construct a standalone ODMN surrogate model tailored to the specific microstructure. This surrogate model then performs the ODMN online prediction algorithm to compute the homogenized mechanical response and the crystallographic texture evolution under any loading path.

The following subsections provide detailed descriptions of each component of the proposed framework. Section 2.1 reviews the original ODMN formulation. Section 2.3 presents the construction of grain-level microstructure graphs. Section 2.4 describes the GNN architecture used to predict micromechanical equilibrium parameters. Section 2.2 details the TACS initialization strategy for texture-related parameters. Section 2.5 introduces the dataset generation process and the computation of ground-truth homogenized stiffness tensors through full-field numerical homogenization. Section 2.6 outlines the offline training procedure for the integrated TACS–GNN–ODMN framework.

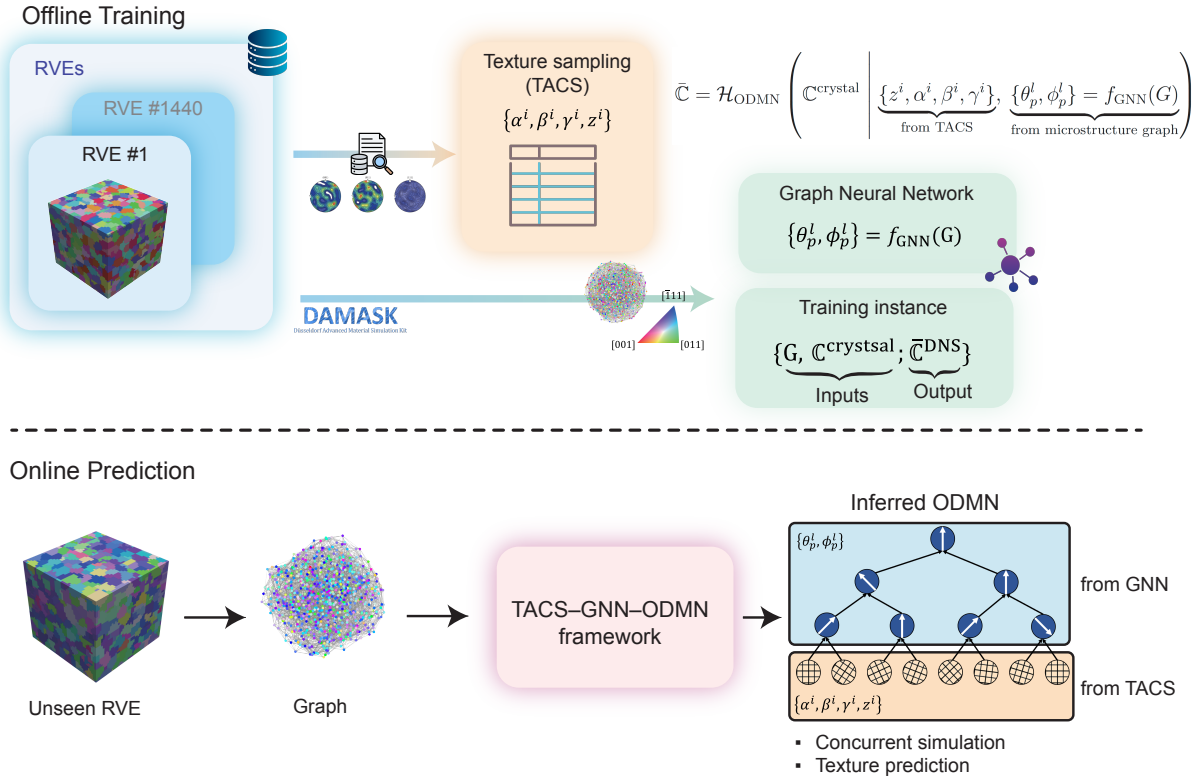


Figure 1: Workflow of the TACS–GNN–ODMN framework. In the offline training stage, polycrystalline RVEs are generated and converted into graphs for GNN-based prediction of micromechanical equilibrium parameters, while TACS provides initialization for texture-related parameters. In the online prediction stage, an unseen RVE is processed to construct a standalone ODMN surrogate, enabling rapid prediction of homogenized responses and texture evolution.

2.1 Overview of the ODMN Architecture

The ODMN is a specialized neural network architecture developed for the homogenization of polycrystalline aggregates. Its formulation is rooted in micromechanical theory, particularly the Hill–Mandel condition and averaging theorems, which allow for the analytical derivation of homogenization functions within each building block. As a result, all trainable parameters in ODMN possess clear physical interpretations [38]. The overall architecture of the ODMN is illustrated in Fig. 2.

ODMN approximates the homogenized response of a RVE by hierarchically decomposing it into multiple subdomains, each represented by a material node. A binary-tree material network defines the hierarchical interaction topology, specifying how these material nodes satisfy stress equilibrium at each tree node. In particular, each tree node is associated with a set of parameters that determine the direction along which the stress-equilibrium condition is enforced.

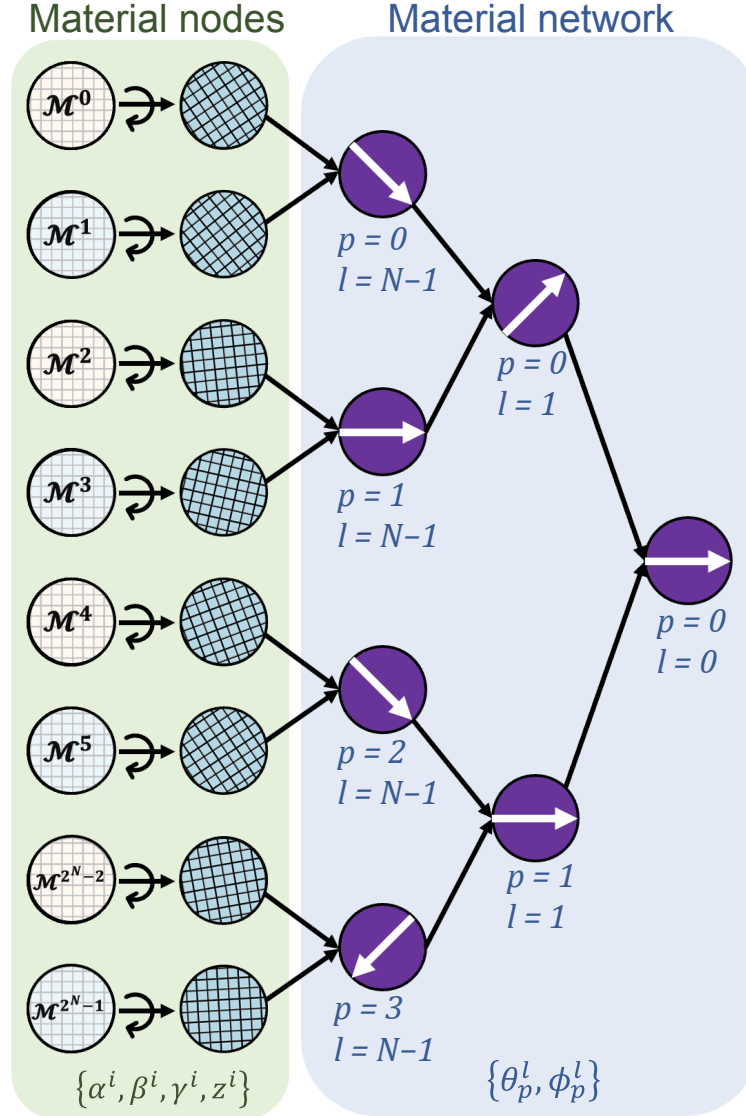


Figure 2: Schematic architecture of the ODMN. A binary-tree material network defines the hierarchical stress-equilibrium interactions, while the 2^N material nodes represent RVE subdomains characterized by local orientations and weighting factors.

The ODMN architecture is governed by a depth hyperparameter N and comprises two principal components:

- A *material network* with N levels, arranged as a binary tree containing $2^N - 1$ tree nodes, each defining an interaction mechanism with the corresponding stress-equilibrium direction.
- A set of 2^N *material nodes*, each representing a subdomain of the RVE and characterized by local orientation and weighting parameters.

Each material node \mathcal{M}^i is parameterized by $\{z^i, \alpha^i, \beta^i, \gamma^i\}$. The scalar z^i is transformed into a non-negative weighting factor W^i via the softplus function:

$$W^i = \text{softplus}(z^i) = \ln(1 + \exp(z^i)), \quad (1)$$

which quantifies the relative contribution of \mathcal{M}^i to the overall RVE response and implicitly governs its role in representing the crystallographic texture.

The angles $\alpha^i, \beta^i, \gamma^i$ are the Tait–Bryan angles that specify the crystallographic orientation of each material node. Each tree node in the material network, representing an interaction mechanism, is parameterized by two rotation angles, θ_p^l and ϕ_p^l , which define the principal directions along which stress equilibrium is enforced at level l and position p . The complete set of trainable parameters \mathcal{F} in an ODMN of depth N is expressed as:

$$\begin{aligned} \mathcal{F} = & \{z^i, \alpha^i, \beta^i, \gamma^i \mid i = 0, 1, \dots, 2^N - 1\} \\ & \cup \{\theta_p^l, \phi_p^l \mid l = 0, 1, \dots, N - 1; p = 0, 1, \dots, 2^l - 1\} \end{aligned} \quad (2)$$

During the offline training stage, the ODMN learns to encode the geometric topology of the RVE through its parameter set \mathcal{F} . Since the ODMN operates under a first-order homogenization framework, linear elastic single-crystal stiffness tensors are sufficient to characterize the material response at the microscale. Accordingly, the analytical homogenization mapping can be expressed as:

$$\bar{\mathbb{C}} = \mathcal{H}_{\text{ODMN}}(\mathbb{C}^{\text{crystal}} \mid \mathcal{F}), \quad (3)$$

where $\bar{\mathbb{C}}$ represents the homogenized stiffness tensor, and $\mathcal{H}_{\text{ODMN}}(\cdot)$ denotes the analytical homogenization operator defined by the ODMN architecture.

2.2 TACS Initialization Strategy

The TACS method [39] is employed to generate a reduced yet statistically representative set of orientations that faithfully captures the original ODF of a polycrystalline aggregate. The procedure begins with K-means clustering in the orientation space, where the optimal number of clusters is determined through a within-cluster sum of squares (WCSS) criterion to balance microstructural resolution and computational efficiency. Within each cluster, a density-aware sampling scheme is applied to ensure that both highly populated and sparsely populated orientation regions are appropriately represented. The reduced orientation set is iteratively refined by comparing its reconstructed ODF histogram with the original one, and the process continues until the relative deviation falls below a prescribed tolerance. The final output is a compact subset of Tait–Bryan angles that statistically reproduces the original ODF.

For an ODMN comprising 2^N material nodes, TACS samples exactly 2^N orientations from the reconstructed ODF. These sampled orientations are directly assigned to the crystallographic orientation parameters $\alpha^i, \beta^i, \gamma^i \mid i = 0, 1, \dots, 2^N - 1$ in the trainable parameter set \mathcal{F} , while the associated weighting factors are initialized uniformly as $z^i = 1$. This initialization establishes a physically consistent and accurate representation of the initial crystallographic texture, thereby enhancing the model’s capability to predict texture evolution during online prediction.

2.3 Microstructure Graph Construction

A graph $G = (V, E)$ is constructed to represent the topological and crystallographic structure of the polycrystalline RVE, where V and E denote the sets of nodes and edges, respectively. Each node corresponds to a grain, while each edge represents the presence of a grain boundary contact between two neighboring grains. The connectivity information is encoded in an adjacency matrix, derived from the shared boundary topology.

Each grain’s crystallographic orientation is reduced to the FCC fundamental zone and represented as a quaternion (q_0, q_1, q_2, q_3) to eliminate the singularities and redundancies associated with Euler angles. In addition to orientation, geometric descriptors are incorporated to capture grain morphology, including the centroid coordinates (x_c, y_c, z_c) , a periodicity flag P_{grain} indicating whether the grain intersects periodic boundaries, and the components of the second moment tensor $(I_{xx}, I_{yy}, I_{zz}, I_{xy}, I_{yz}, I_{zx})$, which characterize shape anisotropy.

Because the TACS-sampled orientations $\{\mathbf{q}_i\}_{i=0}^{2^N-1}$ are permutation-independent and may vary in ordering across different sampling runs even for the same RVE, a consistent correspondence between grains and material nodes must be established. To achieve this, each grain is assigned a permutation-invariant orientation index id_{ori} defined as:

$$\text{id}_{\text{ori}} = \arg \min_i d_{\text{geo}}(\mathbf{q}_{\text{grain}}, \mathbf{q}_i), \quad (4)$$

where the geodesic distance is given by

$$d_{\text{geo}}(\mathbf{q}_a, \mathbf{q}_b) = 2 \arccos(|\langle \mathbf{q}_a, \mathbf{q}_b \rangle|), \quad (5)$$

and $\langle q_a, q_b \rangle$ denotes the quaternion inner product.

This nearest-orientation matching guarantees a deterministic and physically consistent alignment between grains and ODMN material nodes, ensuring that each grain is associated with the most similar crystallographic orientation in the reduced TACS set and eliminating ambiguities arising from the non-deterministic ordering of TACS samples.

The complete set of node features is summarized in Table 1.

Table 1: Grain-level node features for microstructure graph representation.

Feature	Symbol / Unit	Description
Quaternion components	(q_0, q_1, q_2, q_3)	Crystallographic orientation in the FCC fundamental zone, expressed as a unit quaternion
Normalized volume	$V_{\text{grain}}/V_{\text{RVE}}$	Grain volume fraction relative to the RVE
Periodicity flag	P_{grain}	Boolean indicator: 1 if the grain spans a periodic boundary of the RVE, otherwise 0
Centroid coordinates	(x_c, y_c, z_c)	Grain centroid position in Cartesian coordinates
Second moment components	$(I_{xx}, I_{yy}, I_{zz}, I_{xy}, I_{yz}, I_{zx})$	Components of the grain inertia tensor, describing morphological anisotropy
Orientation index	id_{ori}	Index i of \mathbf{q}_i in $\{\mathbf{q}_i\}$ with the minimal geodesic distance to the grain orientation $\mathbf{q}_{\text{grain}}$

2.4 GNN Architecture

The GNN module predicts the micromechanical equilibrium parameters $\{\theta_p^l, \phi_p^l \mid l = 0, 1, \dots, N-1; p = 0, 1, \dots, 2^l-1\}$ in \mathcal{F} from the grain-level microstructure graph, as illustrated in Fig. 3. This parameter set comprises $2(2^N-1) = 2^{N+1}-2$ components, corresponding to the two angular degrees of freedom associated with each internal node of the material network hierarchy.

Two stacked GATv2Conv layers [40] are employed to aggregate information from neighboring grains, with ReLU activation applied after each convolution. Unlike the original Graph Attention Network (GAT), GATv2 introduces a shared linear transformation Θ_s applied to both the source and target node features before the nonlinear attention mapping. This modification allows each query node to independently rank its neighbors, thereby enhancing expressiveness in graphs with complex or irregular connectivity.

The attention coefficient between nodes i and j is computed as

$$\alpha_{ij} = \frac{\exp(a^\top \text{LeakyReLU}(\Theta_s x_i + \Theta_s x_j))}{\sum_{k \in \mathcal{N}(i) \cup \{i\}} \exp(a^\top \text{LeakyReLU}(\Theta_s x_i + \Theta_s x_k))}, \quad (6)$$

where x_i is the feature vector of node i , Θ_s the learnable weight matrix, and a the attention vector. The updated node representation is then

$$x'_i = \sum_{j \in \mathcal{N}(i) \cup \{i\}} \alpha_{ij} \Theta_s x_j. \quad (7)$$

Following the convolutional layers, a global mean pooling operation aggregates node-level embeddings into a fixed-size graph-level feature. This pooled representation is then passed through a regression head consisting of a fully connected layer followed by a Softplus activation function, which ensures smooth nonnegative outputs corresponding to the $2^{N+1}-2$ angular parameters of the material network. The complete architecture is summarized in Table 2.

Table 2: Architecture of the GNN module for predicting ODMN micromechanical equilibrium parameters. B denotes the number of graphs in a batch, and n_{nodes} the number of grains per graph.

Stage	Layer / Operation	Output shape
Input stage	Grain-level feature matrix	$(B, n_{\text{nodes}}, 16)$
Graph convolution stage	GATv2Conv 16 \rightarrow 64, heads = 1	$(B, n_{\text{nodes}}, 64)$
	ReLU activation	$(B, n_{\text{nodes}}, 64)$
	GATv2Conv 64 \rightarrow 64, heads = 1	$(B, n_{\text{nodes}}, 64)$
	ReLU activation	$(B, n_{\text{nodes}}, 64)$
Pooling stage	Global mean pooling	$(B, 32)$
Regression head	Fully connected 32 $\rightarrow (2^{N+1} - 2)$	$(B, (2^{N+1} - 2))$
	Softplus activation ($\beta = 1.0$, threshold = 20.0)	$(B, (2^{N+1} - 2))$

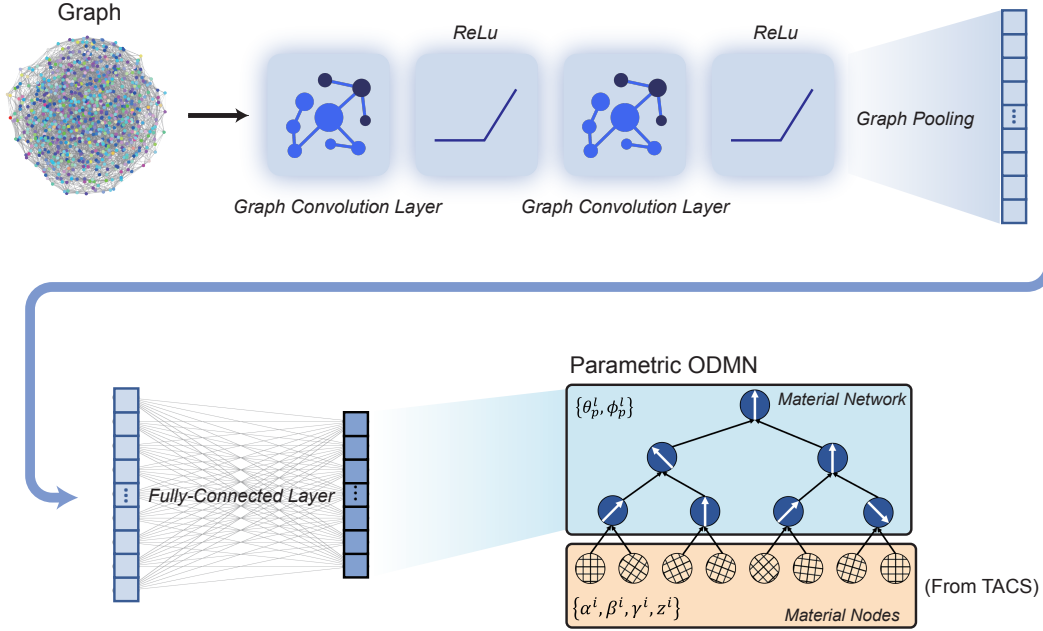


Figure 3: Architecture of the GNN module for predicting ODMN micromechanical equilibrium parameters. A grain-level microstructure graph is processed by two GATv2Conv layers with ReLU activations, followed by global mean pooling and a fully connected layer with Softplus activation to output the angular parameters $\{\theta_p^l, \phi_p^l\}$ of the material network.

2.5 Dataset Preparation

To ensure generalization across diverse microstructures, the training dataset comprises polycrystalline RVEs exhibiting a broad spectrum of crystallographic textures. The texture of each RVE is characterized by the ODF, computed using DREAM.3D (v6.5.171) [41]. In DREAM.3D, the ODF is parameterized for 1,000 uniformly discretized orientations within the FCC fundamental zone, each defined by:

1. *Euler angles*, specifying the crystallographic orientation;
2. *Weight*, expressed in multiples of a random distribution (MRD), where a larger value (e.g., 500,000) indicates a stronger preferred orientation;
3. *Sigma*, defining the spread in Rodrigues space over which the MRD decays quadratically to zero.

For each crystallographic texture, DREAM.3D generated an RVE with approximately 809 grains, discretized into a $45 \times 45 \times 45$ voxel grid. Following the approach of [42], four representative texture types were constructed: (i) Strong-textured-1, one dominant orientation with $Weight = 500,000$, $Sigma = 1$, all others set to $Weight = 1$, $Sigma = 1$; (ii) Strong-textured-2, one dominant orientation with $Weight = 500,000$, $Sigma = 8$, all others set to $Weight = 1$, $Sigma = 1$; (iii) Weak-textured-1, all orientations with $Weight = 1$, $Sigma = 1$; and (iv) Weak-textured-2, two dominant orientations each with $Weight = 500,000$, $Sigma = 10$, all others set to $Weight = 1$, $Sigma = 1$.

For each texture class, 360 distinct ODF realizations were generated, yielding a total of 1,440 RVEs. For each RVE, 500 triplets of elastic constants $\{C_{11}, C_{12}, C_{44}\}$ were independently sampled to construct the corresponding cubic single-crystal stiffness tensors $\mathbb{C}^{\text{crystal}}$ in Voigt notation:

$$\mathbb{C}^{\text{crystal}} = \begin{bmatrix} C_{11} & C_{12} & C_{12} & 0 & 0 & 0 \\ C_{12} & C_{11} & C_{12} & 0 & 0 & 0 \\ C_{12} & C_{12} & C_{11} & 0 & 0 & 0 \\ 0 & 0 & 0 & C_{44} & 0 & 0 \\ 0 & 0 & 0 & 0 & C_{44} & 0 \\ 0 & 0 & 0 & 0 & 0 & C_{44} \end{bmatrix}. \quad (8)$$

The sampling strategy for $\{C_{11}, C_{12}, C_{44}\}$ follows the protocol described in the original ODMN study [38]. Each sampled $\mathbb{C}^{\text{crystal}}$ was then used as input for a direct numerical simulation (DNS) performed with the FFT-based solver in DAMASK, yielding the corresponding homogenized stiffness tensor \mathbb{C}^{DNS} for the given RVE.

In total, 1,280 RVEs were used for training and 160 for validation, evenly distributed across the four texture classes (i.e., 320 training and 40 validation RVEs per class). Each RVE is associated with 500 paired samples $\{\mathbb{C}^{\text{crystal}}, \mathbb{C}^{\text{DNS}}\}$, forming a comprehensive dataset that captures both geometric and mechanical variability. For online prediction assessment, four additional unseen RVEs (one per texture class) were generated and reserved to evaluate the generalization capability of the proposed TACS–GNN–ODMN framework.

2.6 Offline Training Procedure and Online Prediction

The offline training stage jointly optimizes all trainable parameters of the TACS–GNN–ODMN framework in an end-to-end manner, where the GNN module encompasses all learnable weights. For each training sample, the polycrystalline RVE undergoes two parallel preprocessing steps: (i) it is converted into a grain-level microstructure graph G , which is processed by the GNN to predict the micromechanical equilibrium parameters $\{\theta_p^l, \phi_p^l\} \in \mathcal{F}$; and (ii) its ODF is processed by the TACS module to generate 2^N representative crystallographic orientations, which are assigned to the ODMN texture parameters $\alpha^i, \beta^i, \gamma^i$ with uniform weights $z^i = 1$.

The GNN-predicted equilibrium parameters and TACS-derived texture parameters together define a fully parameterized ODMN corresponding to the given microstructure, enabling the analytical homogenization mapping:

$$\bar{\mathbb{C}} = \mathcal{H}_{\text{ODMN}} \left(\mathbb{C}^{\text{crystal}} \left| \underbrace{\{z^i, \alpha^i, \beta^i, \gamma^i\}}_{\text{from TACS}}, \underbrace{\{\theta_p^l, \phi_p^l\}}_{\text{from microstructure graph}} = f_{\text{GNN}}(G) \right. \right), \quad (9)$$

where $\mathbb{C}^{\text{crystal}}$ denotes the cubic single-crystal stiffness tensor of each grain in its local crystal reference frame, and $\bar{\mathbb{C}}$ is the homogenized stiffness tensor predicted by the ODMN.

The predicted homogenized stiffness $\bar{\mathbb{C}}^{\text{ODMN}}$ is compared against the reference value $\bar{\mathbb{C}}^{\text{DNS}}$, obtained from FFT-based full-field simulations in DAMASK [10], through the relative Frobenius norm loss:

$$\mathcal{L} = \frac{1}{N_{\text{batch}}} \sum_{i=1}^{N_{\text{batch}}} \frac{\|\bar{\mathbb{C}}_i^{\text{DNS}} - \bar{\mathbb{C}}_i^{\text{ODMN}}\|^2}{\|\bar{\mathbb{C}}_i^{\text{DNS}}\|^2} \quad (10)$$

All model parameters are optimized using the AdamW algorithm (learning rate 10^{-3} , $\beta_1 = 0.9$, $\beta_2 = 0.98$, weight decay 10^{-4}) for up to 100 epochs, with early stopping triggered when the validation loss no longer improves.

During the online prediction stage, an unseen RVE is processed following the same procedure as in the offline stage: (i) a grain-level graph is constructed and passed through the trained GNN to predict θ_p^l, ϕ_p^l ; and (ii) the ODF is processed

by the TACS module to initialize the texture parameters $\alpha^i, \beta^i, \gamma^i$, again with uniform weights $z^i = 1$. These two components define the complete ODMN model specific to the input microstructure.

Subsequently, the ODMN performs multiscale upscaling and downscaling operations: the macroscopic deformation gradient is downscaled through the network hierarchy to the material nodes, where local constitutive responses (e.g., crystal plasticity) are evaluated under the resolved deformation fields. The resulting stresses and consistent tangent moduli are then upscaled back to the macroscale to determine the homogenized response. The Hill–Mandel condition is imposed to ensure energetic consistency between the micro- and macroscales. If violated, a Newton–Raphson iterative correction is applied, during which successive downscaling and upscaling operations are repeated until convergence. This multiscale procedure allows the ODMN to efficiently approximate the full-field nonlinear mechanical behavior and capture the evolution of crystallographic texture under arbitrary loading conditions, as detailed in our previous work [38].

3 Results and Discussion

3.1 Offline Training Results

The TACS–GNN–ODMN framework was trained with an ODMN depth of $N = 7$. Fig. 4 presents the training and validation error evolution over 100 epochs. Both errors decrease rapidly during the initial epochs, followed by gradual stabilization. The validation error reaches its minimum value of 0.0205 at epoch 35, and the model corresponding to this epoch is adopted for all subsequent evaluations.

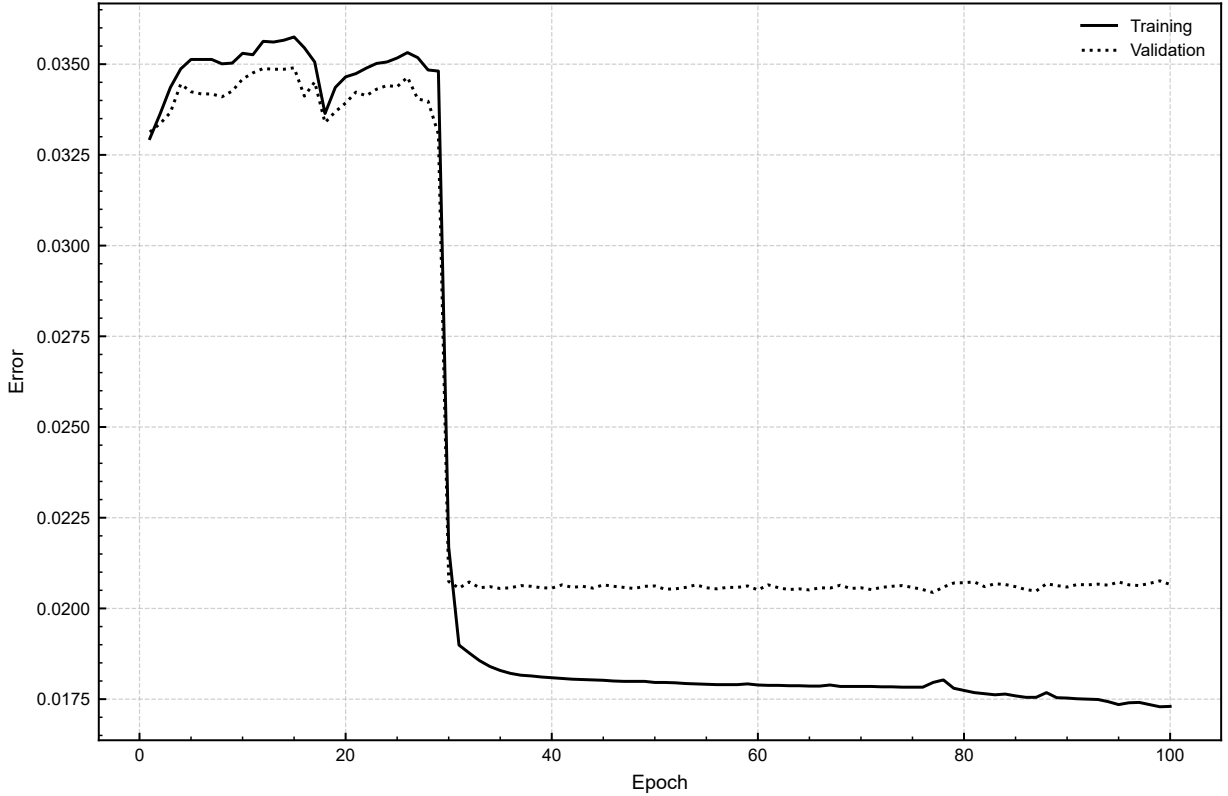


Figure 4: Training and validation error curves of the TACS–GNN–ODMN framework with $N = 7$.

To examine the generalization capability of the trained framework, four unseen polycrystalline RVEs are generated, denoted as S1 (strong-textured-1), S2 (strong-textured-2), W1 (weak-textured-1), and W2 (weak-textured-2), as shown in Fig. 5.

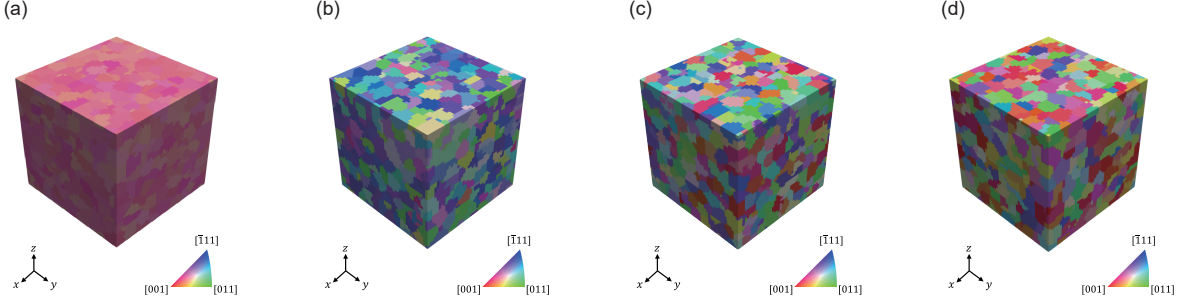


Figure 5: Unseen RVEs used for testing: (a) S1, (b) S2, (c) W1, (d) W2.

Each testing RVE is processed through the TACS–GNN–ODMN framework to construct its corresponding inferred ODMN. The predicted texture parameters $\{\alpha^i, \beta^i, \gamma^i \mid i = 0, 1, \dots, 2^N - 1\}$ are visualized as pole figures to reconstruct the ODFs of the four RVEs. As illustrated in Fig. 6, the reconstructed ODFs exhibit excellent agreement with those obtained from DNS, capturing both the dominant orientation clusters and their dispersion characteristics.

To quantitatively assess the agreement between the reconstructed and DNS-derived ODFs, the normalized texture index of the difference ODF (DODF), \hat{T}^d , is evaluated [43]:

$$\hat{T}^d = \frac{\int [f_{\text{ODMN}}(g) - f_{\text{DNS}}(g)]^2 dg}{\int [f_{\text{DNS}}(g)]^2 dg}, \quad (11)$$

where $f_{\text{ODMN}}(g)$ and $f_{\text{DNS}}(g)$ denote the ODFs obtained from the inferred ODMN prediction and DNS, respectively.

The corresponding \hat{T}^d values for all four RVEs are summarized in Table 3. All cases yield low \hat{T}^d values, confirming the close consistency between ODMN predictions and DNS results. For weakly textured microstructures, the representation tends to be more challenging because their broad orientation distributions are inherently harder to capture using a compact set of representative orientations, a trend consistent with the behavior observed in the original ODMN formulation [38]. Nevertheless, even the weakest case achieves $\hat{T}^d < 0.11$, demonstrating the robustness and transferability of the proposed framework across a wide range of texture intensities.

Table 3: Normalized texture index of the DODF \hat{T}^d quantifying the difference in ODF between the inferred ODMN and DNS results for the four testing RVEs.

Microstructure	\hat{T}^d
S1	0.0001
S2	0.0436
W1	0.1036
W2	0.0847

3.2 Online Prediction Results

In the online prediction stage, the four inferred ODMNs were evaluated under nonlinear deformation using a constitutive framework that integrates the phenomenological crystal plasticity model with the generalized Hooke’s law to represent the elastic–plastic response of the material. Each material node was assigned the constitutive parameters of the AA6022-T4 aluminum alloy [44, 45], an FCC material with 12 slip systems. The corresponding elastic and plastic parameters are summarized in Table 4. The detailed formulation of the crystal plasticity model is presented in Appendix A, and the elastic constitutive relations are given in Appendix B.

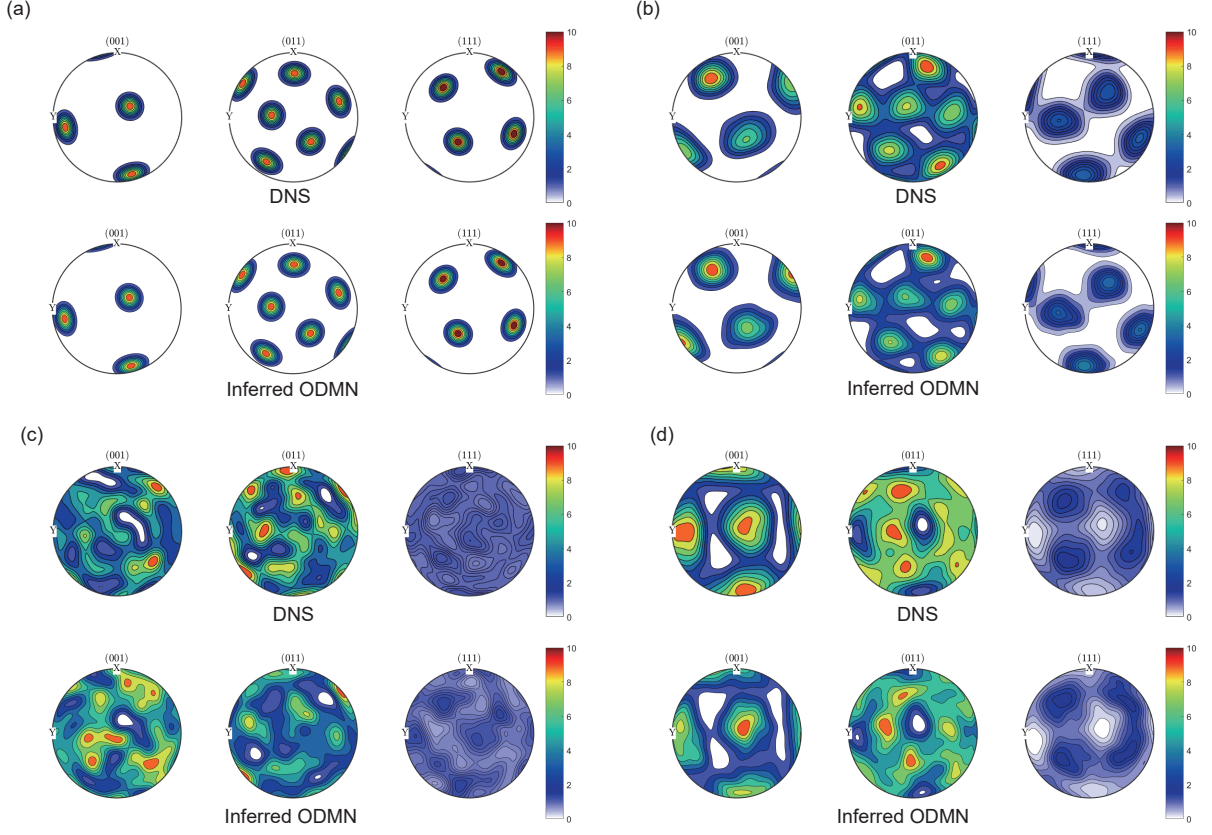


Figure 6: Pole figures of reconstructed ODFs compared with DNS results for the four testing RVEs: (a) S1, (b) S2, (c) W1, and (d) W2.

Table 4: Elastic and plastic material parameters for AA6022-T4 [44, 45].

N_s	$h_0^{\text{sl-sl}}$ (GPa)	ξ_∞^α (MPa)	ξ^0 (MPa)	n	a	$\dot{\gamma}_0$ (s ⁻¹)	h_{int}^α
12	1.02	266	76	20	3.7	0.001	0

C_{11} (GPa)	C_{12} (GPa)	C_{44} (GPa)	$h^{\text{sl-sl}}$
107.3	60.8	28.3	[1, 1, 5.123, 0.574, 1.123, 1.123, 1]

Two loading conditions were examined: uniaxial cyclic loading along the x -direction with a strain rate of $\dot{F}_{11} = 1$, and a simple shear deformation with a strain rate of $\dot{F}_{21} = 1$. For both cases, the ODMN predictions were directly compared against the reference DNS results.

3.2.1 Cyclic loading: mechanical prediction

As shown in Fig. 7, the stress–strain responses predicted by the inferred ODMN exhibit excellent agreement with the DNS results across all four unseen microstructures. To quantitatively assess this agreement, two normalized error metrics—the mean-relative error and the max-relative error—were employed following the established definition in [46]. These metrics systematically evaluate the deviation between the ODMN and DNS stress predictions as:

$$\text{mean-relative error} = \frac{\frac{1}{n} \sum_{i=1}^n |P_i^{\text{DNS}} - P_i^{\text{ODMN}}|}{\max_{i=1, \dots, n} |P_i^{\text{DNS}}|} \quad (12)$$

$$\text{max-relative error} = \frac{\max_{i=1, \dots, n} |P_i^{\text{DNS}} - P_i^{\text{ODMN}}|}{\max_{i=1, \dots, n} |P_i^{\text{DNS}}|} \quad (13)$$

The quantitative performance is summarized in Table 5. Across all RVEs, the mean relative error remains below 2%, demonstrating the high predictive accuracy of the ODMN. The maximum relative error, observed in the S2 RVE, reaches 4.32% but still represents only a slight deviation from the DNS results. These results collectively highlight the robustness of the proposed framework in capturing nonlinear mechanical responses across diverse microstructural textures.

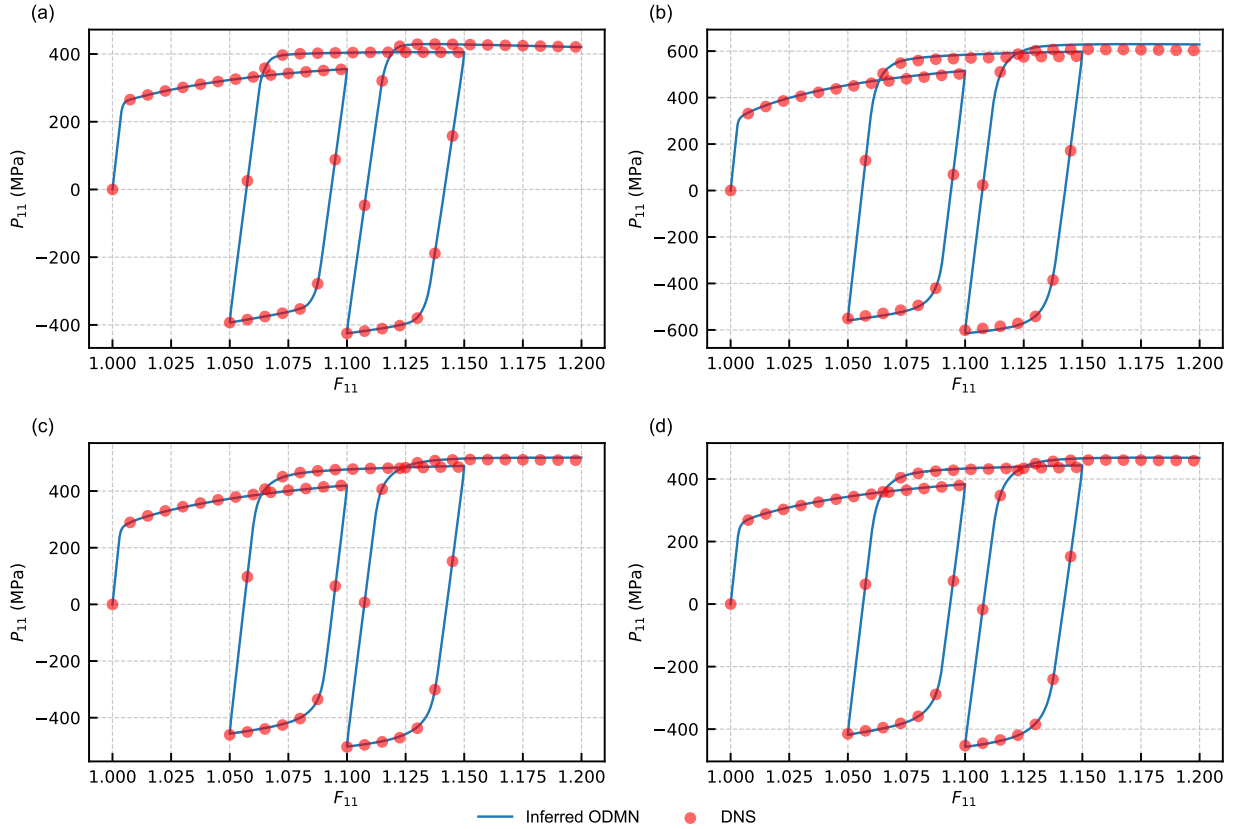


Figure 7: Stress–strain curves under cyclic loading for (a) S1, (b) S2, (c) W1, and (d) W2 at a strain rate of $\dot{F}_{11} = 1$. ODMN predictions are compared with DNS results.

Table 5: Relative stress prediction errors of inferred ODMNs under cyclic loading, compared against DNS results.

RVE	S1	S2	W1	W2
mean-relative error (%)	0.08	1.98	0.50	0.74
max-relative error (%)	0.50	4.32	1.88	2.04

3.2.2 Cyclic loading: texture evolution prediction

The capability of the inferred ODMN to predict texture evolution was evaluated at a deformation of $F_{11} = 1.2$. The resulting textures were visualized as pole figures in Fig. 8, where the predicted results show close agreement with the DNS counterparts across all RVEs.

To quantitatively assess the prediction accuracy, the normalized texture index of the DODF, \hat{T}^d , was employed to measure the deviation between the ODFs predicted by the ODMN and those obtained from DNS. The corresponding values are summarized in Table 6. The results confirm that the inferred ODMN accurately captures texture evolution, particularly in strongly textured RVEs, whereas the deviations become more pronounced in weakly textured ones due to their broader orientation distributions.

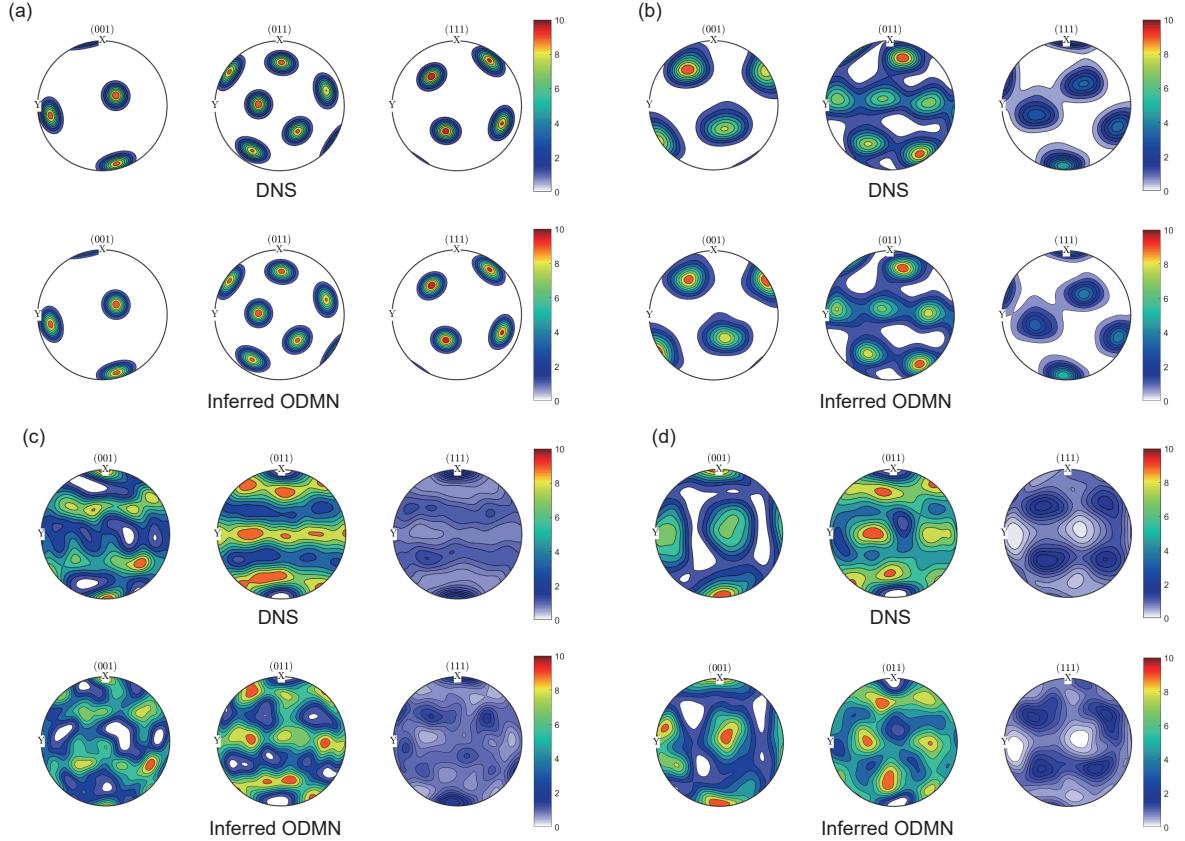


Figure 8: Pole figures after uniaxial cyclic loading with an applied deformation of $F_{11} = 1.2$ (a) S1, (b) S2, (c) W1, and (d) W2. ODMN predictions are compared with DNS results.

Table 6: Normalized texture index of the DODF \hat{T}^d quantifying the difference in ODF between the inferred ODMN model and DNS results under uniaxial loading–unloading with $F_{11} = 1.3$ and a strain rate of $\dot{F}_{11} = 1$.

Microstructure	\hat{T}^d
S1	0.0004
S2	0.0301
W1	0.1176
W2	0.1024

3.2.3 Shear loading: mechanical prediction

The predictive capability of the inferred ODMN was further evaluated under simple shear loading. As shown in Fig. 9, the stress–strain responses predicted by the ODMN exhibit close agreement with the DNS results across all four RVEs.

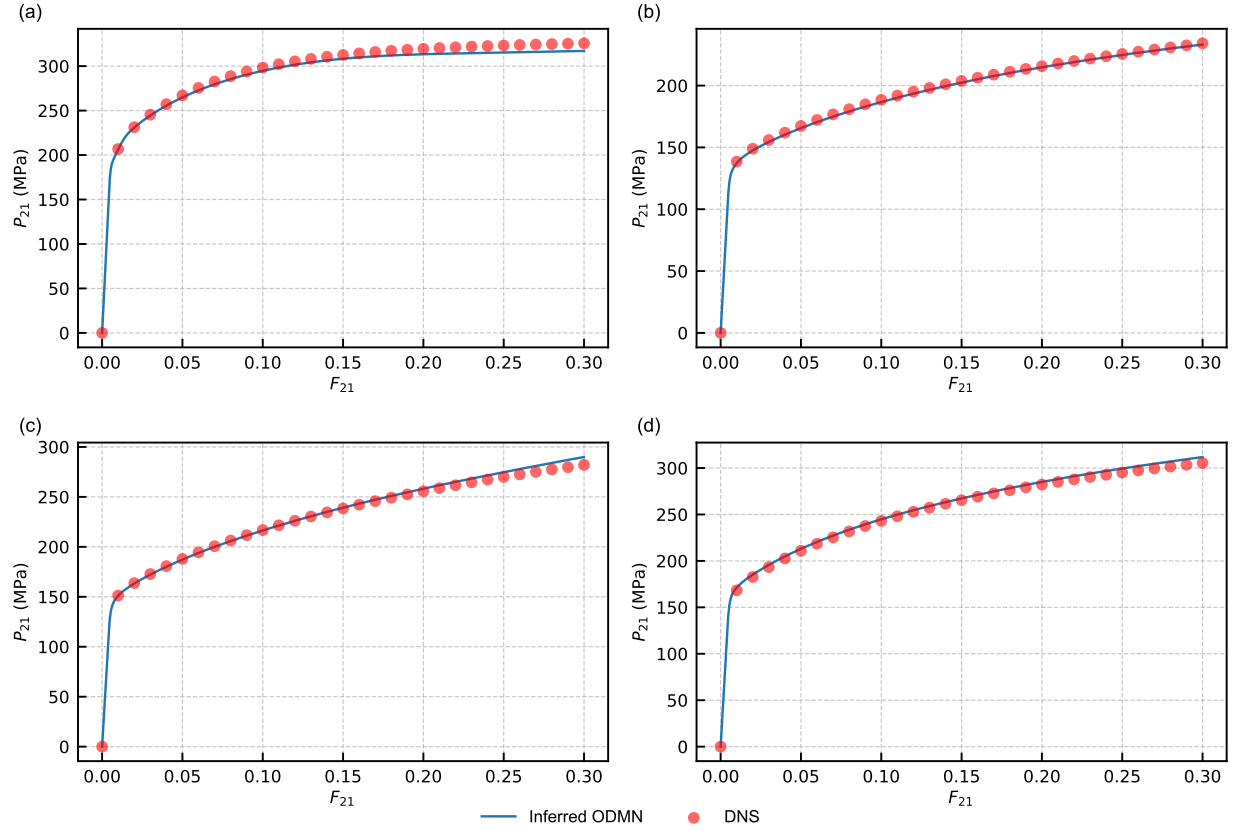


Figure 9: Stress–strain curves under simple shear loading for (a) S1, (b) S2, (c) W1, and (d) W2 at a strain rate of $\dot{F}_{21} = 1$. ODMN predictions are compared with DNS results.

The quantitative performance is summarized in Table 7. Across all RVEs, the mean relative error remains below 1.5%, and the maximum relative error does not exceed 2.8%. These results confirm that the ODMN maintains high predictive accuracy under shear deformation, with only minor deviations from the DNS responses.

Table 7: Relative stress prediction errors of inferred ODMNs under simple shear loading, compared against DNS results.

RVE	S1	S2	W1	W2
mean-relative error (%)	1.44	0.52	0.76	0.93
max-relative error (%)	2.63	0.77	2.78	2.16

3.2.4 Shear loading: texture evolution prediction

Texture evolution under simple shear deformation was evaluated at $F_{21} = 0.3$ with a strain rate of $\dot{F}_{21} = 1$. The pole figures in Fig. 10 compare the DNS and ODMN results, showing that the ODMN captures the evolution of crystallographic texture with good overall accuracy.

To quantitatively assess this agreement, the normalized texture index of the DODF, \hat{T}^d , was employed to measure the deviation in ODF between the ODMN and DNS predictions. The corresponding results, summarized in Table 8, show that \hat{T}^d remains low for strongly textured RVEs, whereas relatively larger discrepancies occur in weakly textured cases. This trend demonstrates that the ODMN effectively captures orientation evolution in strong textures, while its predictions for weak textures, though less precise, remain within acceptable limits.

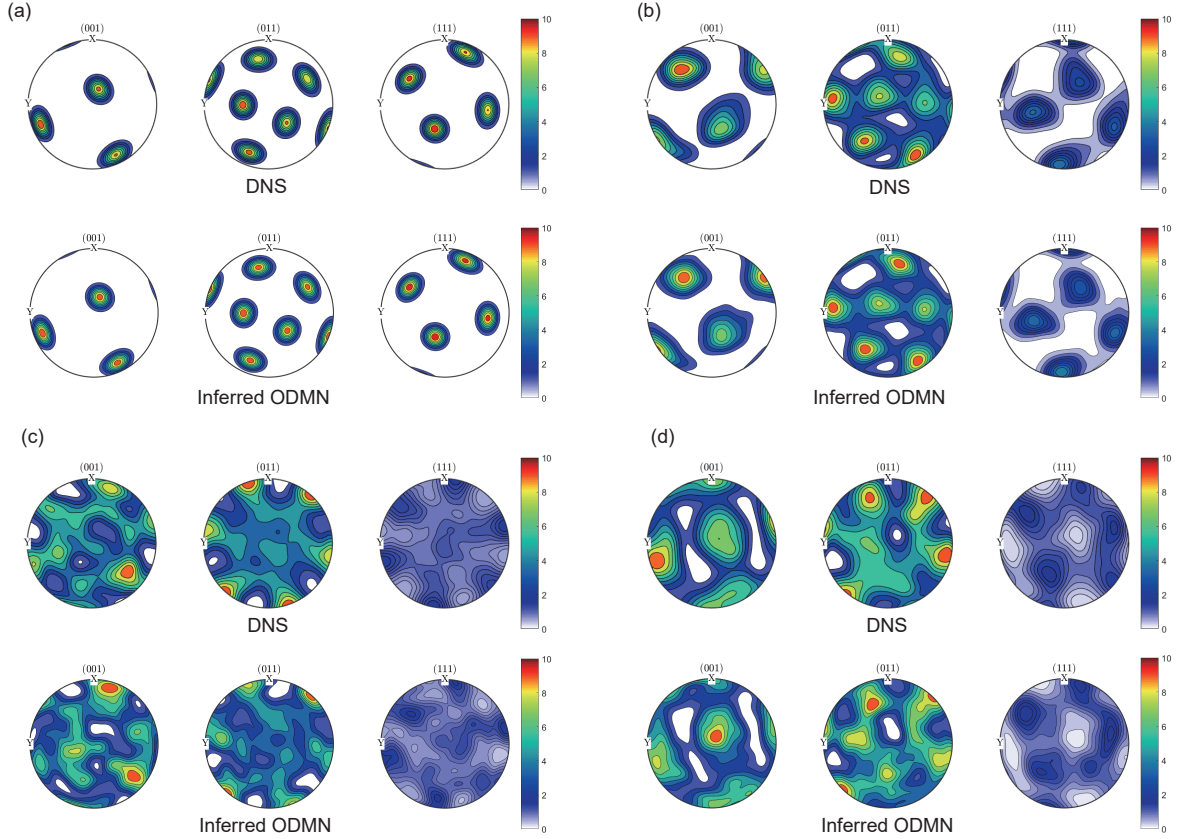


Figure 10: Pole figures after simple shear loading with an applied deformation of $F_{21} = 0.3$: (a) S1, (b) S2, (c) W1, and (d) W2. ODMN predictions are compared with DNS results.

Table 8: Normalized texture index of the DODF \hat{T}^d quantifying the difference in ODF between the inferred ODMN model and DNS results under simple shear deformation with $F_{21} = 0.3$ and strain rate $\dot{F}_{21} = 1$.

Microstructure	\hat{T}^d
S1	0.0101
S2	0.0363
W2	0.0927
W2	0.0911

3.2.5 Summary of online prediction results

Overall, the inferred ODMN exhibits strong predictive performance under both cyclic and shear loading conditions. The stress–strain responses show close agreement with the DNS results, with mean-relative errors consistently below 2% and maximum relative errors remaining within 5%. Regarding texture evolution, the ODMN accurately reproduces the DNS trends in strongly textured RVEs, whereas larger deviations are observed for weakly textured ones under both loading scenarios.

It is worth noting that, as suggested in the original ODMN formulation [38], increasing the number of material nodes could further improve the prediction of texture evolution in weakly textured cases. However, such improvement comes at the expense of computational efficiency, highlighting the trade-off between prediction accuracy and inference speed.

3.3 Investigating the Hyperparameter N in the TACS–GNN–ODMN Framework

To quantitatively evaluate the influence of the hyperparameter N , we performed an ablation study with $N = 6, 7, 8$, and 9. For each configuration, the TACS–GNN–ODMN framework was trained and validated using the same dataset, ensuring a fair comparison across all cases. The corresponding training and validation error curves are shown in Fig. 11.

As anticipated, increasing N consistently reduces the validation error, primarily due to the exponential growth of material nodes (2^N) and the resulting enhancement in representational capacity. In particular, when $N = 9$, the framework achieves a validation error below 1%, confirming its superior representational capability.

Importantly, the choice of N can be systematically tailored to the accuracy requirements of the target application. Smaller values of N lead to simpler network architectures and faster inference, suitable for scenarios where approximate solutions or real-time computations are desired. Conversely, larger values of N provide higher predictive fidelity at the cost of increased computational effort. This tunable architecture thus enables a controllable balance between accuracy and efficiency, allowing the surrogate model to be flexibly adapted to diverse precision and performance demands.

3.4 Inferred ODMN as Reduced Microstructure Interpretation

Owing to the physically interpretable nature of its parameters, the DMN has been shown to provide a reduced yet representative microstructural description, commonly referred to as the analogous unit cell, particularly in composite systems [47]. Conceptually, this analogous unit cell partitions the RVE into 2^N subdomains, each corresponding to a material node in the inferred ODMN. The volume fraction of the i -th subdomain is defined as $\frac{W^i}{\sum_{\forall i} W^i}$, while its crystallographic orientation is parameterized by the Tait–Bryan angles $\alpha^i, \beta^i, \gamma^i$.

The interface normal between subdomains is determined by the stress-equilibrium directions of the material network, denoted as $\vec{\mathbf{N}}_p^l(\theta_p^l, \phi_p^l)$:

$$\vec{\mathbf{N}}_p^l = \begin{bmatrix} \cos(2\pi\phi_p^l) \sin(\pi\theta_p^l) \\ \sin(2\pi\phi_p^l) \sin(\pi\theta_p^l) \\ \cos(\pi\theta_p^l) \end{bmatrix}. \quad (14)$$

In this study, the inferred ODMNs for the four unseen RVEs were reconstructed into their respective analogous unit cells, as shown in Fig. 12.

Each analogous unit cell was discretized into a $45 \times 45 \times 45$ voxel grid, with voxel orientations assigned according to the inferred ODMN parameters. These voxel-based microstructures were then subjected to full-field simulations using the DAMASK-FFT solver under cyclic loading. The material parameters correspond to the AA6022-T4 aluminum alloy (Table 4). The stress–strain responses obtained from these unit-cell DNS calculations were compared against both the original RVE DNS results and the predictions from the inferred ODMN, as shown in Fig. 13. The three responses exhibit close agreement, confirming that the inferred ODMN serves as a reduced-order surrogate capable of

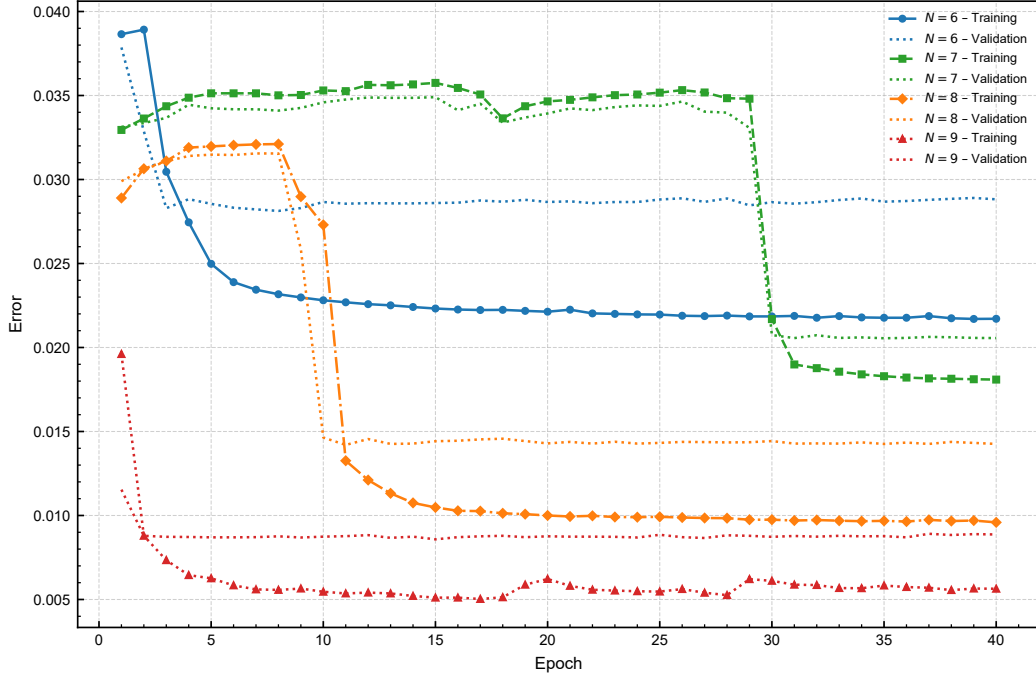


Figure 11: Training and validation errors of the TACS-GNN-ODMN framework for varying values of N .

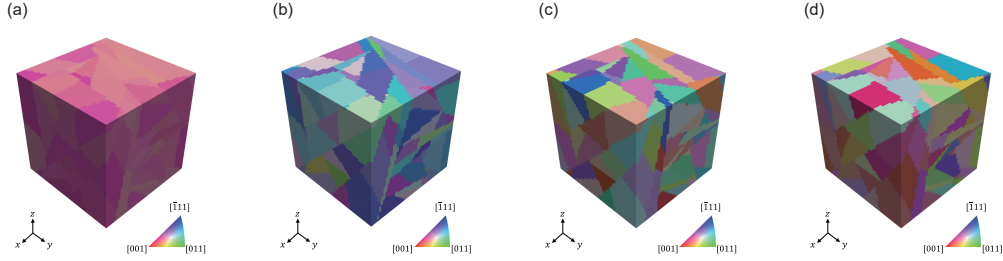


Figure 12: Reconstructed analogous unit cells for the unseen RVEs: (a) S1, (b) S2, (c) W1, and (d) W2.

faithfully reproducing the homogenized mechanical behavior of the original RVEs through physically interpretable microstructural representations.

Beyond the macroscopic response, the local stress distributions were also analyzed. Although the reconstructed analogous unit cells differ from the original RVEs in morphological details, their statistical stress characteristics remain consistent across all three approaches, as shown in Fig. 14 and quantified in Table 9. This observation highlights the capability of the inferred ODMN to not only preserve the global mechanical response but also to replicate the statistical nature of local stress fields through its reduced yet physically grounded representation.

Table 9: Comparison of local stress distributions (P_{11} , in MPa) among the inferred ODMN surrogate, the original RVE DNS, and the analogous unit cell DNS.

	Inferred ODMN	Original RVE	Analogous unit cell
S1	420.41 ± 71.39	420.58 ± 70.54	421 ± 67.42
S2	628.63 ± 146.82	602.34 ± 122.53	617 ± 125.01
W1	517.79 ± 138.98	508.19 ± 134.59	507 ± 140.83
W2	467.79 ± 120.31	458.37 ± 116.22	457.23 ± 113.74

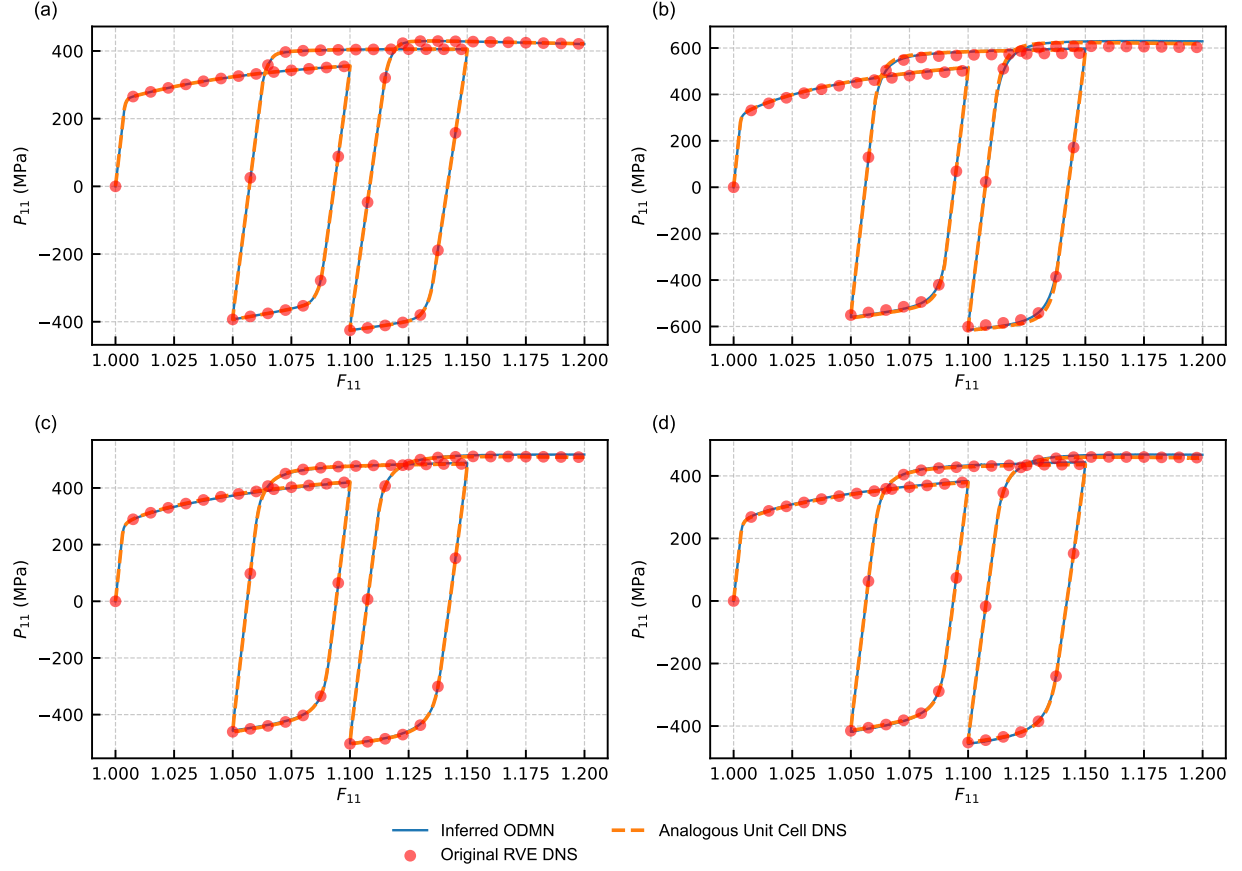


Figure 13: Stress–strain curves under cyclic loading for (a) S1, (b) S2, (c) W1, and (d) W2 at a strain rate of $\dot{F}_{11} = 1$. Comparisons are shown among the original RVE DNS results, the inferred ODMN surrogate predictions, and the analogous unit cell DNS.

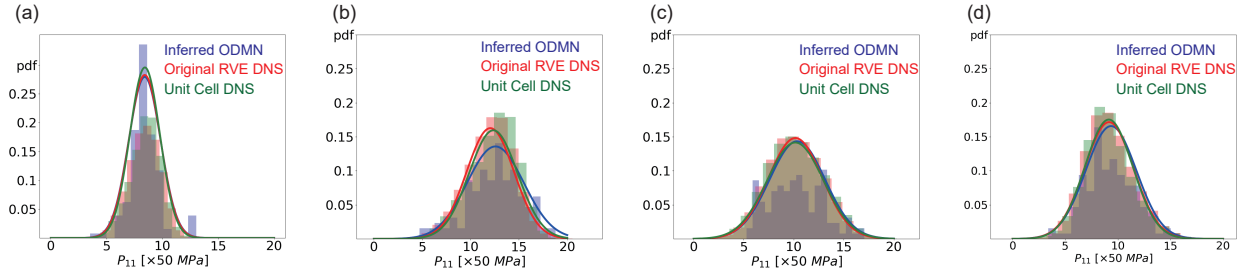


Figure 14: Comparison of local stress distributions predicted by the inferred ODMN surrogate, the original RVE DNS, and the analogous unit-cell DNS under uniaxial tensile loading at $F_{11} = 1.3$ with a strain rate of $\dot{F}_{11} = 1$, for (a) S1, (b) S2, (c) W1, and (d) W2.

The overall consistency among these results demonstrates that the inferred ODMN not only retains the homogenized mechanical response but also accurately reproduces the statistical characteristics of the local stress distributions. Accordingly, the inferred ODMN can be regarded as an interpretable and computationally efficient reduced-order surrogate that encapsulates the essential microstructural physics of the underlying polycrystalline material.

3.5 Computational cost

The training of the TACS–GNN–ODMN framework was performed on an NVIDIA H100 GPU (80 GB HBM3) with a batch size of 512 for 100 epochs, requiring a total of 30 h 40 m 30 s. The online prediction phase was executed on Intel® Xeon® Platinum 8480 (2.0 GHz) CPUs. Table 10 summarizes the wall time required for both the inferred ODMN model and full-field DAMASK FFT simulations under cyclic and shear loading conditions.

Table 10: Wall time (in CPU-seconds) required for online predictions using the inferred ODMN model and full-field DAMASK FFT simulations. Speed-up is computed as the ratio T_{DNS}/T_{ODMN} .

RVE	Inferred ODMN		DAMASK-FFT		Speed-up	
	T_{Cyclic}	T_{Shear}	T_{Cyclic}	T_{Shear}	Cyclic	Shear
S1	3031	2149	782320	604464	258.1×	281.3×
S2	4045	2179	906528	608160	224.1×	279.1×
W1	3717	2373	875952	613648	235.7×	258.6×
W2	3884	2327	871472	615776	224.4×	264.6×

4 Conclusions

This study proposes the TACS–GNN–ODMN framework, an extended formulation of the original ODMN designed to generalize across diverse polycrystalline microstructures without retraining. By integrating the TACS scheme with a GNN, the framework constructs a fully parameterized ODMN surrogate that preserves the physical interpretability and computational efficiency inherent to the original model.

The TACS module provides a data-driven initialization of texture-related parameters by adaptively sampling the ODF, while the GNN infers micromechanical equilibrium parameters from grain-level interaction graphs. This synergistic integration enables the framework to adapt to previously unseen microstructures and to accurately predict both homogenized mechanical responses and crystallographic texture evolution under arbitrary loading paths.

The accuracy and generalization capability of the framework were systematically validated through four case studies involving RVEs with distinct crystallographic textures and loading conditions. The predicted stress–strain responses and texture evolution exhibit excellent agreement with full-field DNS results, confirming both the fidelity and robustness of the proposed approach.

Future research will focus on integrating the TACS–GNN–ODMN framework into broader multiscale modeling pipelines, particularly for establishing structure–process–property linkages at the component scale. Such integration would enable efficient evaluation of microstructural variations induced by manufacturing processes. Moreover, the framework provides a promising foundation for inverse materials design, wherein microstructures can be optimized to achieve target performance objectives.

Acknowledgements

This work is supported by the National Science and Technology Council, Taiwan, under Grant 111-2221-E-002-054-MY3, 112-2221-E-007-028, and 114-2221-E-002-010-MY3. We are grateful for the computational resources and support from the NTUCE-NCREE Joint Artificial Intelligence Research Center and the National Center of High-performance Computing (NCHC).

Declarations

The authors declare that there are no competing interests.

Data Availability

The datasets and trained models used in this study are available upon request from the corresponding author.

Author Contributions

Ting-Ju Wei: Writing – original draft, Methodology, Investigation, Formal analysis, Software, Visualization, Data curation. Tung-Huan Su: Writing – review & editing, Methodology, Formal analysis, Supervision, Investigation, Conceptualization. Chuin-Shan Chen: Writing – review & editing, Supervision, Resources, Project administration, Methodology, Investigation, Funding acquisition, Formal analysis, Conceptualization.

References

- [1] R.A. Lebensohn and C.N. Tomé. A self-consistent anisotropic approach for the simulation of plastic deformation and texture development of polycrystals: Application to zirconium alloys. *Acta Metallurgica et Materialia*, 41(9):2611–2624, 1993.
- [2] Guowei Zhou, Mukesh K. Jain, Peidong Wu, Yichuan Shao, Dayong Li, and Yinghong Peng. Experiment and crystal plasticity analysis on plastic deformation of az31b mg alloy sheet under intermediate temperatures: How deformation mechanisms evolve. *International Journal of Plasticity*, 79:19–47, 2016.
- [3] P.S. Bate and Y.G. An. Plastic anisotropy in aa5005 al–1mg: predictions using crystal plasticity finite element analysis. *Scripta Materialia*, 51(10):973–977, 2004.
- [4] L. Delannay, M.A. Melchior, J.W. Signorelli, J.-F. Remacle, and T. Kuwabara. Influence of grain shape on the planar anisotropy of rolled steel sheets – evaluation of three models. *Computational Materials Science*, 45(3):739–743, 2009. Proceedings of the 17th International Workshop on Computational Mechanics of Materials.
- [5] R.A. Lebensohn and C.N. Tomé. A self-consistent anisotropic approach for the simulation of plastic deformation and texture development of polycrystals: Application to zirconium alloys. *Acta Metallurgica et Materialia*, 41(9):2611–2624, 1993.
- [6] P.A. Turner and C.N. Tomé. A study of residual stresses in zircaloy-2 with rod texture. *Acta Metallurgica et Materialia*, 42(12):4143–4153, 1994.
- [7] H. Wang, P.D. Wu, C.N. Tomé, and Y. Huang. A finite strain elastic–viscoplastic self-consistent model for polycrystalline materials. *Journal of the Mechanics and Physics of Solids*, 58(4):594–612, 2010.
- [8] D D Tjahjanto, P Eisenlohr, and F Roters. A novel grain cluster-based homogenization scheme. *Modelling and Simulation in Materials Science and Engineering*, 18(1):015006, dec 2009.
- [9] D D Tjahjanto, P Eisenlohr, and F Roters. Multiscale deep drawing analysis of dual-phase steels using grain cluster-based rgc scheme. *Modelling and Simulation in Materials Science and Engineering*, 23(4):045005, apr 2015.
- [10] F. Roters, M. Diehl, P. Shanthraj, P. Eisenlohr, C. Reuber, S.L. Wong, T. Maiti, A. Ebrahimi, T. Hochrainer, H.-O. Fabritius, S. Nikolov, M. Friák, N. Fujita, N. Grilli, K.G.F. Janssens, N. Jia, P.J.J. Kok, D. Ma, F. Meier, E. Werner, M. Stricker, D. Weygand, and D. Raabe. Damask – the düsseldorf advanced material simulation kit for modeling multi-physics crystal plasticity, thermal, and damage phenomena from the single crystal up to the component scale. *Computational Materials Science*, 158:420–478, 2019.
- [11] I. Temizer and P. Wriggers. An adaptive multiscale resolution strategy for the finite deformation analysis of microheterogeneous structures. *Computer Methods in Applied Mechanics and Engineering*, 200(37):2639–2661, 2011. Special Issue on Modeling Error Estimation and Adaptive Modeling.
- [12] P. Eisenlohr, M. Diehl, R.A. Lebensohn, and F. Roters. A spectral method solution to crystal elasto-viscoplasticity at finite strains. *International Journal of Plasticity*, 46:37–53, 2013. Microstructure-based Models of Plastic Deformation.
- [13] P. Shanthraj, P. Eisenlohr, M. Diehl, and F. Roters. Numerically robust spectral methods for crystal plasticity simulations of heterogeneous materials. *International Journal of Plasticity*, 66(SI):31–45, MAR 2015.
- [14] A. Vidyasagar, Abbas D. Tutcuoglu, and Dennis M. Kochmann. Deformation patterning in finite-strain crystal plasticity by spectral homogenization with application to magnesium. *Computer Methods in Applied Mechanics and Engineering*, 335:584–609, JUN 15 2018.
- [15] Ricardo A. Lebensohn and Anthony D. Rollett. Spectral methods for full-field micromechanical modelling of polycrystalline materials. *Computational materials science*, 173, FEB 15 2020.

- [16] Lallit Anand. Single-crystal elasto-viscoplasticity: application to texture evolution in polycrystalline metals at large strains. *Computer Methods in Applied Mechanics and Engineering*, 193(48):5359–5383, 2004. Advances in Computational Plasticity.
- [17] Milan Ardeljan, Irene J. Beyerlein, and Marko Knezevic. A dislocation density based crystal plasticity finite element model: Application to a two-phase polycrystalline hcp/bcc composites. *Journal of the Mechanics and Physics of Solids*, 66:16–31, 2014.
- [18] Milan Ardeljan, Irene J. Beyerlein, and Marko Knezevic. Effect of dislocation density-twin interactions on twin growth in az31 as revealed by explicit crystal plasticity finite element modeling. *International Journal of Plasticity*, 99:81–101, 2017.
- [19] S.R. Kalidindi, C.A. Bronkhorst, and L. Anand. Crystallographic texture evolution in bulk deformation processing of fcc metals. *Journal of the Mechanics and Physics of Solids*, 40(3):537–569, 1992.
- [20] Marko Knezevic, Amanda Levinson, Ryan Harris, Raja K. Mishra, Roger D. Doherty, and Surya R. Kalidindi. Deformation twinning in az31: Influence on strain hardening and texture evolution. *Acta Materialia*, 58(19):6230–6242, 2010.
- [21] Marko Knezevic, Mark R. Daymond, and Irene J. Beyerlein. Modeling discrete twin lamellae in a microstructural framework. *Scripta Materialia*, 121:84–88, 2016.
- [22] Franz Roters, Philip Eisenlohr, Thomas R Bieler, and Dierk Raabe. *Crystal Plasticity Finite Element Methods: In Materials Science and Engineering*. John Wiley & Sons, Ltd, 2010.
- [23] Xinxin Sun, Hongwei Li, Mei Zhan, Junyuan Zhou, Jian Zhang, and Jia Gao. Cross-scale prediction from rve to component. *International Journal of Plasticity*, 140:102973, 2021.
- [24] Olga Ibragimova, Abhijit Brahme, Waqas Muhammad, Julie Lévesque, and Kaan Inal. A new ann based crystal plasticity model for fcc materials and its application to non-monotonic strain paths. *International Journal of Plasticity*, 144:103059, 2021.
- [25] Guowei Zhou, Yuanzhe Hu, Zizheng Cao, Myoung Gyu Lee, and Dayong Li. A physics-constrained neural network for crystal plasticity modelling of fcc materials. *Scripta Materialia*, 241:115861, 2024.
- [26] Colin Bonatti and Dirk Mohr. On the importance of self-consistency in recurrent neural network models representing elasto-plastic solids. *Journal of the Mechanics and Physics of Solids*, 158:104697, 2022.
- [27] Colin Bonatti, Bekim Berisha, and Dirk Mohr. From cp-fft to cp-rnn: Recurrent neural network surrogate model of crystal plasticity. *International Journal of Plasticity*, 158:103430, 2022.
- [28] Yuanzhe Hu, Guowei Zhou, Myoung-Gyu Lee, Peidong Wu, and Dayong Li. A temporal graph neural network for cross-scale modelling of polycrystals considering microstructure interaction. *International Journal of Plasticity*, 179:104017, 2024.
- [29] Zeliang Liu and C.T. Wu. Exploring the 3d architectures of deep material network in data-driven multiscale mechanics. *Journal of the Mechanics and Physics of Solids*, 127:20–46, 2019.
- [30] Sebastian Gajek, Matti Schneider, and Thomas Böhlke. On the micromechanics of deep material networks. *Journal of the Mechanics and Physics of Solids*, 142:103984, 2020.
- [31] Van Dung Nguyen and Ludovic Noels. Micromechanics-based material networks revisited from the interaction viewpoint; robust and efficient implementation for multi-phase composites. *European Journal of Mechanics - A/Solids*, 91:104384, 2022.
- [32] Ludovic Noels et al. Interaction-based material network: A general framework for (porous) microstructured materials. *Computer Methods in Applied Mechanics and Engineering*, 389:114300, 2022.
- [33] Dongil Shin, Peter Jefferson Creveling, Scott Alan Roberts, and Rémi Dingreville. Deep material network for thermal conductivity problems: Application to woven composites. *Computer Methods in Applied Mechanics and Engineering*, 431:117279, 2024.
- [34] Benedikt Sterr, Sebastian Gajek, Andrew Hrymak, Matti Schneider, and Thomas Böhlke. Deep material networks for fiber suspensions with infinite material contrast. *International Journal for Numerical Methods in Engineering*, 126(7):e70014, 2025.
- [35] Jimmy Gaspard Jean, Tung Huan Su, Szu Jui Huang, Cheng-Tang Wu, and Chuin Shan Chen. Graph-enhanced deep material network: multiscale materials modeling with microstructural informatics. *Computational Mechanics*, 75:113–136, 2025.
- [36] Wen-Ning Wan, Ting-Ju Wei, Tung-Huan Su, and Chuin-Shan Chen. Decoding material networks: exploring performance of deep material network and interaction-based material networks. *Journal of Mechanics*, 40:796–807, 2024.

- [37] Ting-Ju Wei and Chuin-Shan Chen. Foundation model for composite microstructures: Reconstruction, stiffness, and nonlinear behavior prediction. *Materials & Design*, 257:114397, 2025.
- [38] Ting-Ju Wei, Tung-Huan Su, and Chuin-Shan Chen. Orientation-aware interaction-based deep material network in polycrystalline materials modeling. *Computer Methods in Applied Mechanics and Engineering*, 441:117977, 2025.
- [39] J Wanni, CA Bronkhorst, and DJ Thoma. Machine learning enhanced analysis of ebsd data for texture representation. *npj Computational Materials*, 10(1):133, 2024.
- [40] Shaked Brody, Uri Alon, and Eran Yahav. How attentive are graph attention networks? *arXiv preprint arXiv:2105.14491*, 2021.
- [41] Michael A Groeber and Michael A Jackson. Dream. 3d: a digital representation environment for the analysis of microstructure in 3d. *Integrating materials and manufacturing innovation*, 3(1):56–72, 2014.
- [42] Wei Dai, Huamiao Wang, Qiang Guan, Dayong Li, Yinghong Peng, and Carlos N Tomé. Studying the micromechanical behaviors of a polycrystalline metal by artificial neural networks. *Acta Materialia*, 214:117006, 2021.
- [43] Saiyi Li, Irene J. Beyerlein, David J. Alexander, and Sven C. Vogel. Texture evolution during multi-pass equal channel angular extrusion of copper: Neutron diffraction characterization and polycrystal modeling. *Acta Materialia*, 53(7):2111–2125, 2005.
- [44] Timothy J. Barrett and Marko Knezevic. Deep drawing simulations using the finite element method embedding a multi-level crystal plasticity constitutive law: Experimental verification and sensitivity analysis. *Computer Methods in Applied Mechanics and Engineering*, 354:245–270, 2019.
- [45] Max-Planck-Institut für Eisenforschung GmbH. Damask documentation: Phenopowerlaw aa6022-t4, 2024. Accessed: 21st June 2024.
- [46] Tianyu Huang, Zeliang Liu, CT Wu, and Wei Chen. Microstructure-guided deep material network for rapid nonlinear material modeling and uncertainty quantification. *Computer Methods in Applied Mechanics and Engineering*, 398:115197, 2022.
- [47] Dongil Shin, Ryan Alberdi, Ricardo A Lebensohn, and Rémi Dingreville. Deep material network via a quilting strategy: visualization for explainability and recursive training for improved accuracy. *npj Computational Materials*, 9(1):128, 2023.

Appendix A Phenomenological Crystal Plasticity Model

In this work, the phenomenological crystal plasticity framework is adopted as the local constitutive law to capture the material response. The implementation follows the formulation available in DAMASK and neglects the effect of deformation twinning [10]. The plastic velocity gradient \mathbf{L}_p is expressed as the accumulated contribution of all slip systems α :

$$\mathbf{L}_p = \sum_{\alpha} \dot{\gamma}^{\alpha} (\mathbf{s}_s^{\alpha} \otimes \mathbf{n}_s^{\alpha}) \quad (\text{A.1})$$

where \mathbf{s}_s^{α} denotes the unit vector of the slip direction, \mathbf{n}_s^{α} the slip plane normal, and $\dot{\gamma}^{\alpha}$ the shear rate of slip system α .

The evolution of slip resistance ξ^{α} is modeled as a hardening law that governs its transition from the initial value ξ_0^{α} toward the saturation value ξ_{∞}^{α} :

$$\dot{\xi}^{\alpha} = h_0^{s-s} (1 + h_{\text{int}}^{\alpha}) \times \sum_{\alpha'}^{N_s} \left| \dot{\gamma}^{\alpha'} \right| \left| 1 - \frac{\xi^{\alpha'}}{\xi_{\infty}^{\alpha'}} \right|^a \text{sgn} \left(1 - \frac{\xi^{\alpha'}}{\xi_{\infty}^{\alpha'}} \right) h^{\alpha\alpha'} \quad (\text{A.2})$$

The slip rate $\dot{\gamma}^{\alpha}$ is defined in terms of the resolved shear stress τ^{α} and the slip resistance ξ^{α} as

$$\dot{\gamma}^{\alpha} = \dot{\gamma}_0^{\alpha} \left| \frac{\tau^{\alpha}}{\xi^{\alpha}} \right|^n \text{sgn}(\tau^{\alpha}) \quad (\text{A.3})$$

The resolved shear stress τ^{α} is obtained from Schmid's law using the Mandel stress \mathbf{M}^p :

$$\tau^{\alpha} = \mathbf{M}^p \cdot (\mathbf{s}^{\alpha} \otimes \mathbf{n}^{\alpha}) \quad (\text{A.4})$$

Appendix B Generalized Hooke's law

The elastic response of the material is represented through the generalized form of Hooke's law. It establishes the relation between the second Piola–Kirchhoff stress tensor \mathbf{S} and the Green–Lagrange strain tensor \mathbf{E} via the fourth-order stiffness tensor \mathbb{C} :

$$\mathbf{S} = \mathbb{C} : \mathbf{E} \quad (\text{B.5})$$

where

- \mathbf{S} is the second Piola–Kirchhoff stress tensor, measured in the reference configuration;
- \mathbb{C} denotes the fourth-order elastic stiffness tensor, characterizing the elastic constants of the material;
- \mathbf{E} is the Green–Lagrange strain tensor.

The Green–Lagrange strain tensor \mathbf{E} is defined directly in terms of the elastic deformation gradient, \mathbf{F}^e , as:

$$\mathbf{E} = \frac{1}{2} ((\mathbf{F}^e)^T \mathbf{F}^e - \mathbb{I}) \quad (\text{B.6})$$

with

- \mathbf{F}^e representing the elastic part of the deformation gradient, i.e., the reversible deformation,
- \mathbb{I} being the second-order identity tensor.